Journal of Alloys and Metallurgical Systems 5 (2024) 100051

Contents lists available at ScienceDirect

Journal of Alloys and Metallurgical Systems

journal homepage: www.journals.elsevier.com/journal-of-alloys-and-metallurgical-systems

Crystal structure and physical properties of the new $AcNi_6Si_6$ compounds (*Ac*: Th, U)

A. Martinelli [a,*,1], G. Lamura [a,2], P. Solokha [b,3], A. Provino [b,4], C. Bernini [a,5], M. Ceccardi [c,6], M. Pani [b,7], M. Ferretti [b,8], S.K. Dhar [d,9], P. Manfrinetti [a,b,10]

[a] Institute SPIN-CNR, 16152 Genova, Italy
[b] Department of Chemistry, University of Genova, 16146 Genova, Italy
[c] Department of Physics, University of Genova, 16146 Genova, Italy
[d] Department of Condensed Matter Physics and Materials Science, T.I.F.R., 400005 Mumbai, India

ARTICLE INFO

Keywords:
Actinide intermetallics
$AcNi_6Si_6$
Crystal structure
Group theory
Electrical resistivity
Magnetic properties

ABSTRACT

The crystal structure of the new ternary $ThNi_6Si_6$ and UNi_6Si_6 intermetallic compounds has been investigated by means of both single crystal and powder X-ray diffraction followed by Rietveld refinement. Both compounds adopt the tetragonal $CeNi_6Si_6$-type structure, crystallizing in the space group *P4/nbm* (No. 125) (Pearson's symbol *tP*52). This prototype is a ternary defect-derivative of the binary $NaZn_{13}$-type. A group-theoretical analysis carried out in this work illustrates the structural relationship occurring among the aristotype $NaZn_{13}$-type, the partially disordered $CeNi_6Si_6$ and the fully ordered YNi_6Si_6 hettotype crystal structures.

Zero-field low-temperature electrical resistivity data show a metallic behaviour for both materials. DC magnetic measurements from room temperature down to 2 K reveal diamagnetic behaviour for $ThNi_6Si_6$, indicating that Ni atoms do not carry any magnetic moment. On the other hand, the effective magnetic moment per formula unit for UNi_6Ni_6 is found to be $\mu_{eff} = 3.07(1)\ \mu_B$, suggesting a trivalent (U^{3+}) or tetravalent (U^{4+}) state for U atoms with partial delocalization of 5 *f* electrons. No magnetic ordering down to 2 K is seen in UNi_6Si_6. No superconducting transition was detected, neither in UNi_6Si_6 nor in $ThNi_6Si_6$ in the available temperature interval ($2\ K \leq T \leq 300\ K$).

1. Introduction

Heavy-fermions superconductors (HFSs) are unconventional superconductors containing rare earth (*R*) or actinide (*Ac*) as one of the constituent elements, where the hybridization of the *f*-electrons with the normal conduction electrons near the Fermi level is responsible for their unusual and peculiar physical behaviour. The first HFSs that were discovered are $CeCu_2Si_2$ [1] and UBe_{13} [2,3] and since then many other Ce and U based HFSs were identified and characterized.

UBe_{13} is one of the most interesting HFSs ($T_c = 0.9$ K) because the superconductivity appears from a state characterized by a strongly temperature-dependent electrical resistivity [4]. This compound crystallizes in the cubic $NaZn_{13}$-type structure [Pearson's symbol *cF*112, space group $Fm\bar{3}c$ (No. 226)] [2,5], which is also the pristine prototype of several ternary compounds such as the RNi_6Si_6. Previous systematic

* Corresponding author.
E-mail address: alberto.martinelli@spin.cnr.it (A. Martinelli).
[1] ORCID 0000-0001-8391-3486
[2] ORCID 0000-0001-5629-1319
[3] ORCID 0000-0002-5252-635X
[4] ORCID 0000-0002-7577-6642
[5] ORCID 0000-0003-4807-0924
[6] ORCID 0000-0001-7977-7215
[7] ORCID 0000-0002-4711-1504
[8] ORCID 0000-0003-0709-3281
[9] ORCID 0000-0003-3074-9058
[10] ORCID 0000-0002-3346-5619

https://doi.org/10.1016/j.jalmes.2023.100051
Received 26 October 2023; Received in revised form 7 December 2023; Accepted 16 December 2023
Available online 19 December 2023

structural investigations on RNi_6Si_6 compounds identified two different ternary prototype derivative of $NaZn_{13}$: $CeNi_6Si_6$-type (*tP*52, *P4/nbm*, No. 125) and YNi_6Si_6-type (*tP*52, $P\bar{4}b2$, No. 117) [6,7]. It was ascertained that the $CeNi_6Si_6$-type structure is adopted only for R = La and Ce, whereas the YNi_6Si_6 prototype is formed by R = Y, Nd, Sm, Gd, Tb, Dy, Ho, Er, Tm and Yb. Although both prototypes show two Wyckoff sites for the R atoms (2*a* and 2*b* for the former and 2*c* and 2*d* for the latter), the two structures differ from each other in the ordering of Ni and Si atoms. In the $CeNi_6Si_6$-type, two out of the four 8 *m* sites are occupied by Ni atoms and the other two 8 *m* sites are filled by Si atoms; the remaining 16 *n* site is randomly occupied by both Ni and Si in a ratio 50:50% [1]. In the YNi_6Si_6-type, Ni atoms fully occupy three 8*i* positions and Si atoms fill three additional 8*i* sites with a full occupation factor; thus, giving rise to an ordered crystal structure [1].

We were interested to explore if heavy-fermion superconductivity occurs in the ternary derivatives of uranium based $NaZn_{13}$-type compounds, besides the already well known UBe_{13} [2,3]. In this regard, we synthesized and characterized alloys on the composition $U(Ni,Si)_{13}$ and, as a result, we identified the new UNi_6Si_6 compound. As the Th-substituted UBe_{13} system, $U_{1-x}Th_xBe_{13}$, has been found to have a more intriguing unconventional superconductivity than the parent UBe_{13} compound [8], for as a comparison we also synthesized and investigated the non-magnetic counterpart $ThNi_6Si_6$. Therefore, in this work, we will discuss the crystal structure, electrical resistivity and magnetic properties of the newly identified UNi_6Si_6 and $ThNi_6Si_6$ silicide compounds.

2. Materials and experimental methods

The polycrystalline samples (total mass ≈ 2–3 g) were prepared by arc melting the elements weighed in stoichiometric proportion, under a static TiZr-gettered Ar atmosphere. The starting metals used were commercial high-purity products; the purities were: 99.7 wt% for Th, 99.9 wt% for depleted U, 99.99 wt% for Ni and 99.9999 wt% for Si. The surface of depleted U was cleaned in nitric acid in a chemical hood before arc melting. Weighing and handling of all samples were carried out inside a glove-box under an Ar atmosphere. The buttons were melted three times, turning them upside down each time to ensure their homogenization. The total weight loss after melting was less than 0.3 wt%. After melting, the ingots were placed inside sealed-under-Ar outgassed Ta crucibles, and then sealed under vacuum in silica ampoules. Annealing was carried out in a resistance furnace at high temperature (800 °C–1000 °C) for 7–8 days. Samples were then slowly cooled down inside the furnace (not quenched).

Phase analysis was performed by optical and scanning electron microscopy (SEM) (Leica Cambridge S360), in conjunction with an energy-dispersive X-ray (EDX) microprobe (Oxford X-Max 20) for semi-quantitative elemental analysis. The micrographic specimens were prepared by standard polishing technique of a vertical section of the samples. Both the EDX analysis on the overall area of the specimens and known binary line compounds present as secondary or impurity phases were used as references to check for the accuracy of the elemental analyses, which, in this way, was estimated to be within 0.5 at% for U, Th, Ni and Si.

Single crystals were selected from fragments of the sample crushed in a mortar and affixed to a glass fiber with grease. A complete dataset was obtained in a routine manner at ambient conditions on a three-circle Bruker D8 QUEST diffractometer with PHOTON III photon counting detector equipped by the graphite monochromatized Mo Kα ($\lambda = 0.71073$ Å) radiation, operating in ω-scan mode. Intensity data were collected over the reciprocal space up to ≈ 36° in θ (achieving a ≈ 0.6 Å resolution) with exposures of 10 s per frame. Data collection was performed, and the unit cell was initially refined, using APEX4 [9]. Successively, data were reduced using SAINT [10] and XPREP [11]. Lorentz, polarization, and absorption effects were corrected using SADABS [12]. The structure was solved and refined with the aid of SHELXL-2019/1 [13].

Powder X-ray diffraction (PXRD) patterns were collected on either a Stoe Guinier camera (Cu $K_{\alpha1}$ radiation and Si as an internal (a = 5.4308 Å) or on a X'Pert PRO Philips diffractometer (Cu $K_{\alpha1}$ radiation; data collected over the range $10° \leq 2\theta \leq 100°$, with a step size of 0.02°). The Guinier powder patterns were indexed with the aid of LAZY PULVERIX [14] and accurate lattice parameters obtained by using least squares methods. Structural refinements by Rietveld method were carried out using the FullProf software [15].

DC magnetisation data both as a function of temperature and applied magnetic field were collected using a commercial Magnetic Properties Measurement System (SQUID, Quantum Design, Inc., USA), whereas electrical resistivity as a function of temperature, ρ(T), was measured in between 2 and 300 K by the standard four-probe technique using the AC transport option of a Physical Properties Measurement System (PPMS, Quantum Design, Inc. USA).

3. Group-theoretical analysis

In order to discuss the group-theoretical analysis carried out in this work, it is worthwhile to highlight again that the RNi_6Si_6 compounds crystallize in either the tetragonal $CeNi_6Si_6$-type (*tP*52, *P4/nbm*, No. 125) for *RE* = La and Ce or in the tetragonal YNi_6Si_6-type (*tP*52, $P\bar{4}b2$, No. 117) for R = Y, Nd, Sm, Gd, Tb, Dy, Ho, Er, Tb and Yb [6,7]. Both structural models are defect derivatives of the $NaZn_{13}$ structure type, the latter being isotypic with the heavy-fermion superconductor UBe_{13} [2,3].

In particular, a *translationgleiche* transition of index 3 transforms the cubic structure of $NaZn_{13}$ (*cF*112; $Fm\bar{3}c$) into the tetragonal structure of $LaCo_9Si_4$ (*tI*56, *I4/mcm*, No. 140) (Fig. 1). A further *klassengleiche* transition of index 2 yields the $CeNi_6Si_6$ structure (*tP*52, *P4/nbm*, No 125), from which the YNi_6Si_6 structure (*tP*52, $P\bar{4}b2$, No. 117) is finally obtained by a *translationgleiche* transition of index 2. In particular, Co atoms are found at three different Wyckoff sites in the $LaCo_9Si_4$ structure: 16 *l*, 16*k* and 4*d*. The 16 *l* site splits into two different 8 *m* sites in the $CeNi_6Si_6$ structure (which are occupied by Ni and Si atoms, respectively), whereas the 16*k* site is transformed into the 16 *n* site, where Ni and Si atoms are randomly distributed. Conversely, no corresponding site can be found for the 4*d* site; as a consequence the $CeNi_6Si_6$ structure is a defective derivative of the $LaCo_9Si_4$ structure. The ordering of the Ni and Si atoms in the 16 *n* site of the $CeNi_6Si_6$ structural model leads to the formation of the YNi_6Si_6 structure type, where Ni and Si atoms are distributed in separated 8*i* sites (Fig. 1 and Fig. 2). Whatever the adopted crystal structure is, the R atoms are in an irregular snub-cube coordination.

4. Results and discussion

4.1. SEM observation and EDX analysis

The microstructure of the UNi_6Si_6 sample after annealing at 800 °C is characterized by elongated grains constituted by both UNi_6Si_6 in the outer region and a new phase with composition UNi_2Si_3 in the inner core (Fig. 3, left panel). The matrix, in which the elongated grains are dispersed, is constituted by the binary NiSi phase, within which very thin grains of the UNi_6Si_6 precipitate are still visible (Fig. 3, right panel).

Interestingly, after a thermal annealing at 1000 °C the sample contained mainly the UNi_6Si_6 compound; the UNi_2Si_3 phase was still present as a secondary phase in limited regions of the alloy, but no trace of the binary NiSi phase was observed (Fig. 4). This result suggests that a higher annealing temperature is needed for the formation of UNi_6Si_6 and preparation of single phase materials.

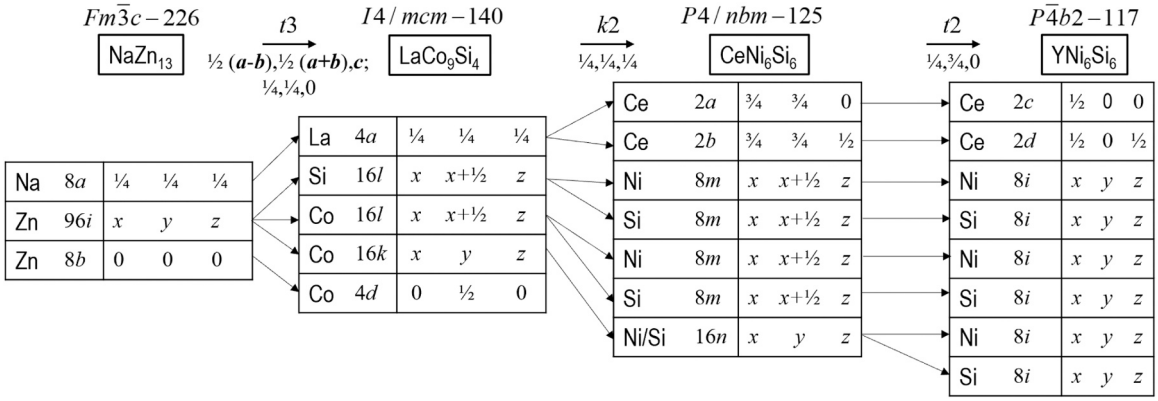

Fig. 1. Group-subgroup transformations from the cubic $NaZn_{13}$ structure to the tetragonal YNi_6Si_6 one; transformation type (*t*: *translationgleiche*; *k*: *klassengleiche*), transformation index and origin shift are indicated.

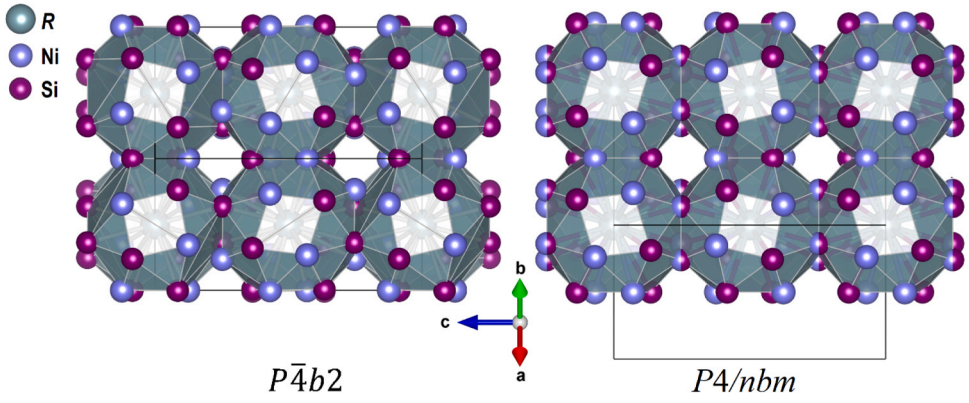

Fig. 2. Representation of the YNi_6Si_6 (on the left) and $CeNi_6Si_6$ (on the right) structure types; the atomic coordination around the *R* atoms is highlighted.

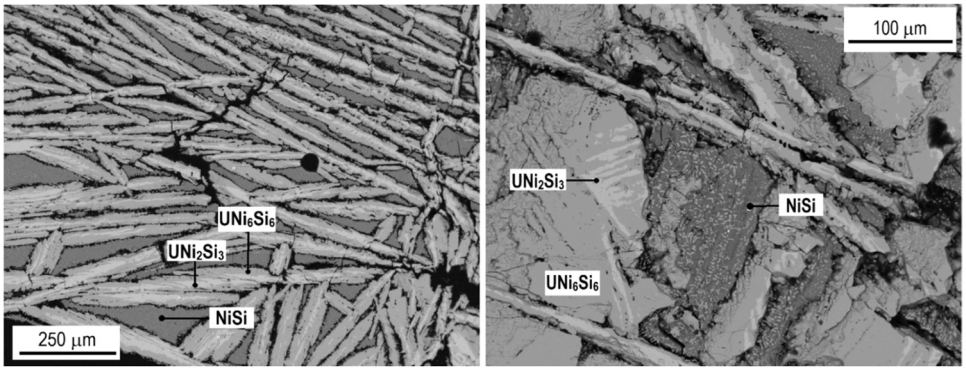

Fig. 3. SEM microphotographs [backscattered electrons (BSE) mode] showing the microstructure of the UNi_6Si_6 sample after thermal annealing at 800 °C; two different magnifications of the sample are shown. The grey phase surrounding the elongated grains (outer region) is UNi_6S_6, while the light grey phase (elongated grains, as inner core) is UNi_2Si_3; the darker matrix is made up of NiSi containing thin precipitates of UNi_6Si_6.

4.2. Single-crystal X-ray diffraction

A total of 2725 frames were collected for UNi_6Si_6 single crystal dataset. The integration of the data using a primitive tetragonal unit cell yielded a total of 29690 reflections of which 884 were independent (average redundancy 33, completeness of 99.9%, R_{int} = 4.26%, R_{sig} = 1.33%). Analysis of systematic absences performed by XPREP [11] clearly indicates *P4/nbm* (n° 125) as the only possible space group type (see Table 1).

At this point, a preliminary structural model was derived by direct methods giving a reasonable result. UNi_6Si_6 crystallizes in the $CeNi_6Si_6$-type structure, with space group type *P4/nbm* (No. 125) and 52 atoms per unit cell *tP*52. The U atoms are situated in a 2*a* and 2*b* sites (occupied by Ce atoms in $CeNi_6Si_6$) and the four 8 *m* sites are fully occupied by two Ni and two Si species, respectively. The only 16 *n* Wyckoff position available in the structure clearly indicates the statistical mixture of Ni/Si to be very close to 1:1 ratio. Further EXYZ and EADP restrictions were applied during the refinement for this position [16]. The final anisotropic refinement converged to comparably good residuals of *R*1 = 0.017, *wR*2 = 0.037 and *GOF* = 1.14; this is complemented by a flat difference Fourier map with residual electron densities lower then 2 $e^-/Å^3$. The single crystal and refinement details are collected in Table 2;

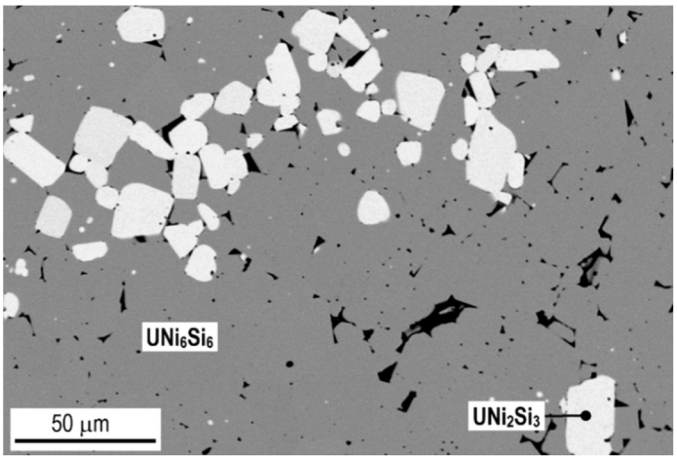

Fig. 4. SEM microphotograph (BSE mode) showing the microstructure of the UNi_6Si_6 sample after thermal annealing at 1000 °C; the dark grey grains pertain to the UNi_6Si_6 phase while the white grains are the UNi_2Si_3 phase. The analysis was carried out on a selected area of the specimen rich in the secondary phase UNi_2Si_3.

the final refined atomic coordinates and thermal parameters, $U_{eq,}$ are collected in Table 3. The corresponding CIF file has been deposited at the Cambridge Database with the following depository number: CSD-2189461.

The interatomic distances for $d_{obs}/\Sigma r_M \leq 1.376$ (where d_{obs} is the observed interatomic distance and Σr_M is the sum of the single metallic radius, r_M) and atomic coordination numbers (CN) for UNi_6Si_6 are listed in Table 4. The first coordination sphere around U atoms features pseudo Frank-Kasper polyhedra with CN = 24 and composition $U@Ni_{12}Si_{12}$ for both U1 (in 2*a*) and U2 (in 2*b*) atoms, respectively. The U−Ni, U−Si and U−Ni/Si interatomic distance values range between 3.130 Å and 3.260 Å, all of them showing values of $d_{obs}/\Sigma r_M > 1$ (Table 4). The shortest interatomic distances in this structure are formed between Ni−Si and Ni−Ni/Si atoms; these values range between 2.301 Å and 2.628 Å, and all of them are lower than the sum of their corresponding metallic radii ($d_{obs}/\Sigma r_M < 1$). In particular, the atomic coordination around the two Ni atoms (in 8 *m*) is characterized by icosahedra with CN = 12 and composition $Ni@U_2Ni_5Si_5$ and $Ni@U_2Ni_3Si_7$ for Ni1 and Ni2 atoms, respectively; the atomic coordination around the two Si atoms (in 8 *m*) is also characterized by icosahedra with CN = 12 and composition $Si@U_2Ni_5Si_5$ for Si1 and $Si@U_2Ni_7Si_3$ for Si2. The atomic coordination around Ni/Si atoms (in 16 *n*) is described again by icosahedra with CN = 12 and a composition of $(Ni/Si)@U_2Ni_5Si_5$.

4.3. X-ray powder diffraction analysis and Rietveld refinement

In order to confirm the results obtained by single crystal X-ray diffraction, both structural models of the $CeNi_6Si_6$ and the YNi_6Si_6-type were tested by Rietveld refinement method PXRD data collected for UNi_6Si_6 and $ThNi_6Si_6$. For $ThNi_6Si_6$, no good quality crystals were available to perform a single crystal investigation. Therefore, its crystal structure was refined by Rietveld method only. The two Rietveld refinement fits are shown in Fig. 5a and b, respectively.

As a result, although the difference in the *R*-factors for both structural models is low, the $CeNi_6Si_6$ structural model (*P4/nbm*; *tP*52) provides the best result in terms of agreement factors for both compounds (R_B = 3.43 and 3.89 and R_F = 3.84 and 4.55 for UNi_6Si_6 and $ThNi_6Si_6$ adopting the $CeNi_6Si_6$-type structure against R_B = 3.91 and 4.00 and R_F = 4.21 and 4.81 for the two compounds adopting the YNi_6Si_6-type

Table 2
Details of the UNi_6Si_6 crystal structure investigation and refinement at ambient conditions.

Formula Weight [g/mol]	758.702
Structural prototype	$CeNi_6Si_6$
Pearson symbol	*tP*52
Crystal system	Tetragonal
Space group	*P4/nbm* (No. 125)
a [Å]	7.7507(1)
c [Å]	11.1202(3)
Unit cell volume [Å^3]	668.03(2)
Z	4
Calculated density, ρ [g/cm^3]	7.5
Absorption coefficient, μ [mm^{-1}]	41.7
F(000)	1376
Crystal description	irregular form
Theta range [°]	3.664° ≤ ϑ ≤ 36.270°
Index ranges *h*, *k*, *l*	$-12 \leq h \leq 12$ $-12 \leq k \leq 12$ $-18 \leq l \leq 18$
Reflections collected	29690
Independent reflections	884
Absorption correction	multi-scan method
Refinement method	Full-matrix least-squares on F^2
Data/parameter	884/40
Goodness of fit (*GOF*) on F^2	1.14
Final *R* indices [$I > 2\sigma(I)$]	$R1 = 0.017$, $wR2 = 0.037$
R indices (all data)	$R1 = 0.024$, $wR2 = 0.039$
R_{int}/R_{sym}	0.043/0.013
Largest diff. peak and hole [e$^-$/Å^3]	+ 1.90, –0.96

Table 3
Atomic coordinates (standardized setting) and isotropic displacement parameters (U_{eq}) for UNi_6Si_6 as obtained from single-crystal investigation.

Atom	Wyckoff site	*x*	*y*	*z*	Occ.	U_{eq} [Å^2]
U1	2*a*	¼	¼	0	1	0.00619(7)
U2	2*b*	¼	¼	½	1	0.00662(7)
Ni1	8 *m*	0.61702 (5)	0.38298 (5)	0.07226 (5)	1	0.0102(1)
Ni2	8 *m*	0.57865 (5)	0.07865 (5)	0.37619 (6)	1	0.0143(1)
Si1	8 *m*	0.63014 (11)	0.13014 (11)	0.57818 (12)	1	0.0122(2)
Si2	8 *m*	0.58827 (11)	0.41173 (11)	0.86725 (11)	1	0.0106(2)
Ni3	16 *n*	0.44423 (8)	0.19084 (7)	0.75035 (5)	0.498(4)	0.0116(1)
Si3	16 *n*	0.44423 (8)	0.19084 (7)	0.75035 (5)	0.502(4)	0.0116(1)

Table 1
Systematic absence exceptions for UNi_6Si_6 dataset.

Symmetry elements	$4^1/4^3$	4^2	n–	-b-	-c-	-n-	-2_1-	–c
Total	77	52	866	2335	2257	2258	93	1455
N ($I > 3$)	68	46	2	46	742	728	0	793
$\langle I \rangle$	51.7	34.6	0.3	0.4	4.1	4.0	0.2	5.9
$\langle I/\sigma \rangle$	15.7	15.3	0.5	0.7	3.6	3.5	0.5	4.9

N = number of reflections that should be absent for the corresponding lattice centering type;
N ($I > 3$) = number of reflections that are observed but should be absent;
$\langle I \rangle$ = mean intensity; $\langle I/\sigma \rangle$ = mean intensity divided by sigma.

Table 4
Interatomic distances for $d_{obs}/\Sigma r_M \leq 1.135$ and atomic coordination numbers (CN) in UNi_6Si_6 ($CeNi_6Si_6$-type, *tP*52, *P4/nbm*).

Central atom	Ligands	d [Å]	$d_{obs}/\Sigma r_M$	Central atom	Ligands	d [Å]	$d_{obs}/\Sigma r_M$
U1 (2*a*)	8 Ni1	3.1305(4)	1.116	Si1 (8 *m*)	1 Ni2	2.3160(15)	0.903
(CN = 24)	8 Ni3/Si3	3.1912(6)	1.123	(CN = 9)	1 Ni2	2.3442(10)	0.914
	8 Si2	3.2595(9)	1.132		2 Ni2	2.3476(10)	0.915
					2 Ni3/Si3	2.4420(13)	0.939
U2 (2*b*)	8 Ni2	3.1856(5)	1.135		2 Si1	2.5447(16)	0.965
(CN = 24)	8 Ni3/Si3	3.1979(6)	1.125		1 Si1	2.6276(12)	0.996
Ni1 (8 *m*)	1 Si2	2.3014(13)	0.897	Si2 (8 *m*)	1 Ni1	2.3014(13)	0.897
(CN = 8)	1 Si2	2.3486(10)	0.916	(CN = 9)	1 Ni1	2.3486(10)	0.916
	2 Si2	2.3916(10)	0.932		2 Ni1	2.3916(10)	0.932
	2 Ni3/Si3	2.4520(8)	0.970		2 Ni3/Si3	2.4223(11)	0.931
	2 Ni1	2.6138(6)	1.049		2 Ni3/Si3	2.5364(11)	0.975
					1 Ni2	2.7092(14)	1.056
Ni2 (8 *m*)	1 Si1	2.3160(15)	0.903				
(CN = 13)	1 Si1	2.3442(10)	0.914	Ni3/Si3 (16 *n*)	2 Ni3/Si3	2.2255(8)	0.867
	2 Si1	2.3476(10)	0.915	(CN = 9)	1 Si2	2.4223(11)	0.944
	2 Ni3/Si3	2.5015(8)	0.989		1 Si1	2.4420(13)	0.952
	2 Ni3/Si3	2.5247(8)	0.998		1 Ni1	2.4520(8)	0.984
	1 Si2	2.7092(14)	1.056		1 Ni2	2.5015(7)	1.004
					1 Ni2	2.5247(7)	1.013
					1 Si2	2.5364(11)	0.989
					1 Ni3/Si3	2.7031(8)	1.054

structure (Table 5). However, another important consideration is worth to be noted: while in the YNi_6Si_6-type structure there are 20 independent structural parameters to be refined (18 at. positions + 2 lattice parameters), there are only 13 independent structural parameters (11 at. positions + 2 lattice parameters) in the $CeNi_6Si_6$ structural model. As a consequence, the fitting improvement obtained with the $CeNi_6Si_6$-type is much more significant than that obtained with the YNi_6Si_6-type which must, therefore, be rejected.

Structural data refined by Rietveld method for UNi_6Si_6 are in fair agreement with those obtained by single-crystal X-ray diffraction analysis. Table 6 lists the atomic coordinates and structural parameters obtained from Rietveld refinement on $ThNi_6Si_6$. Trace amount of secondary phases are detected in both samples: $NiSi_2$ (≈ 1.0 vol%) for the $ThNi_6Si_6$ sample and UNi_2Si_3 (≈ 5.5 vol%) for the UNi_6Si_6 sample. The lattice parameters and the unit cell volumes obtained from the Rietveld refinement on both compounds [$a = 7.7498(1)$ Å, $c = 11.1186(1)$ Å, $V_{cell} = 667.78(1)$ Å^3 for UNi_6Si_6 and $a = 7.8021(1)$ Å, $c = 11.1636(1)$ Å, $V_{cell} = 679.56(1)$Å^3 for $ThNi_6Si_6$] are in agreement with the expected trend on the basis of the tabulated atomic volume of U and Th (20.73 Å^3 and 32.95 Å^3 for U and Th, respectively [17]): the unit cell of UNi_6Si_6 being smaller than that of $ThNi_6Si_6$. Moreover, the volume of formation (or contraction volume) {ΔV %, where $\Delta V = [(V_{obs} - V_{calc})/V_{calc} \times 100]$; V_{calc} is the volume of the compound calculated from the atomic volumes of the individual atoms [17]} calculated for both compounds is − 19.2% for UNi_6Si_6 and − 22.3% for $ThNi_6Si_6$. The ΔV % is proportional to the formation enthalpy of a compound. As the volume of formation is quite negative for both compounds, this indicates their formation to be thermodynamically favoured; moreover, the value for $ThNi_6Si_6$ is even lower than that of the homolog UNi_6Si_6, thus suggesting $ThNi_6Si_6$ to be more stable than UNi_6Si_6.

The crystal structure of UNi_6Si_6 is strictly related to that of UNi_7Si_6. In fact, UNi_7Si_6 crystallizes with the $LaCo_9Si_4$-type structure (*tI*56, *I*4/*mcm*) (Fig. 1), where Wyckoff sites with multiplicity equal to 16 (two 16 *l* and one 16*k*) are all disorderly occupied by both Ni and Si atoms [18]. In this context, the crystal structure of UNi_6Si_6 can be therefore considered as a partially ordered defect-derivative of the UNi_7Si_6 structure.

Combining the structural data reported for RNi_6Si_6 compounds in previous works [6,7] with those obtained in the present study about UNi_6Si_6 and $ThNi_6Si_6$, a structural map (Fig. 6) can be drawn by plotting the atomic size ratio defined as $SZ_{aMD}/(SZ_{aMD})_{max}$ (see Villars *et al.* [19] for the detailed definition of this quantity) of the rare earth or actinide element as a function of the unit cell volume. From this plot, it is evident how the stability of the *P4/nbm* and $P\bar{4}b2$ structures is proportionally dependent on the atomic size of the rare earth or actinide element. According to Villars *et al.* [19], the partially disordered $CeNi_6Si_6$-type structure is more stable for larger atomic sizes, whereas the ordered YNi_6Si_6 -type structure forms for lower atomic sizes.

4.4. Physical properties measurements

The temperature dependence of the zero-field cooled (ZFC) mass magnetic susceptibility, $\chi_m(T)$, of UNi_6Si_6 sample was measured between 2 and 300 K by applying a magnetic field H = 10 kOe; the data are presented in Fig. 7. As the field-cooled (FC) data are completely superposed to the ZFC ones, they were omitted for sake of clarity. The $\chi_m(T)$ data follow a paramagnetic Curie-like behavior from 300 K down to about 60 K where an anomaly occurs at 40–60 K suggesting the presence of a magnetic transition. Below such transition $\chi_m(T)$ still shows a Curie-like *T*-dependence. The predominance of a paramagnetic-like behavior is confirmed also by $1/\chi_m(T)$ data displayed in the lower panel of Fig. 7: $1/\chi_m(T)$ is clearly linear with almost the same slope except in the 40 K < T < 70 K range where the above mentioned transition takes place.

It is worth to note that UNi_6Si_6 sample contains a small amount (5.5 vol%, as detected from Rietveld refinement) of a new ternary UNi_2Si_3 as extra phase. In order to determine the values of Curie-Weiss temperature (θ) and effective magnetic moment (μ_{eff}) for UNi_6Si_6 we took into account the results obtained from the magnetic measurements on pure samples of UNi_2Si_3. Both structural and magnetic properties of such new phase will be the object of a next article. We performed a two component Curie-Weiss fit in the range 100–300 K (red line in upper panel of Fig. 7) by the following model function:

$$\chi_m(T) = \chi_0 + w \bullet \frac{C_1}{T-\theta_1} + (1-w) \bullet \frac{C_2}{T-\theta_2} \quad (1)$$

where χ_0 is a T-constant contribution, $w = 0.055$ is the relative weight of the spurious phase (5.5 vol%, as determined by Rietveld refinement) and $C_1 = 231(1) \bullet 10^{-5} \frac{emu \bullet K}{g \bullet Oe}$ is the Curie constant as determined by a Curie-Weiss fit above the magnetic ordering temperature on a pure sample of UNi_2Si_3. Such value corresponds to an effective magnetic moment of $\mu_{exp} = 2.85(4)$ μ_B ascribed to the U-free magnetic ions of UNi_2Si_3. $\theta_1 = +5(1)$ K represents the Curie-Weiss temperature of UNi_2Si_3. By fixing the parameters of such impurity phase (w, C_1 and θ_1) we could determine the Curie-Weiss temperature $\theta_2 = -20(6)$ K, the

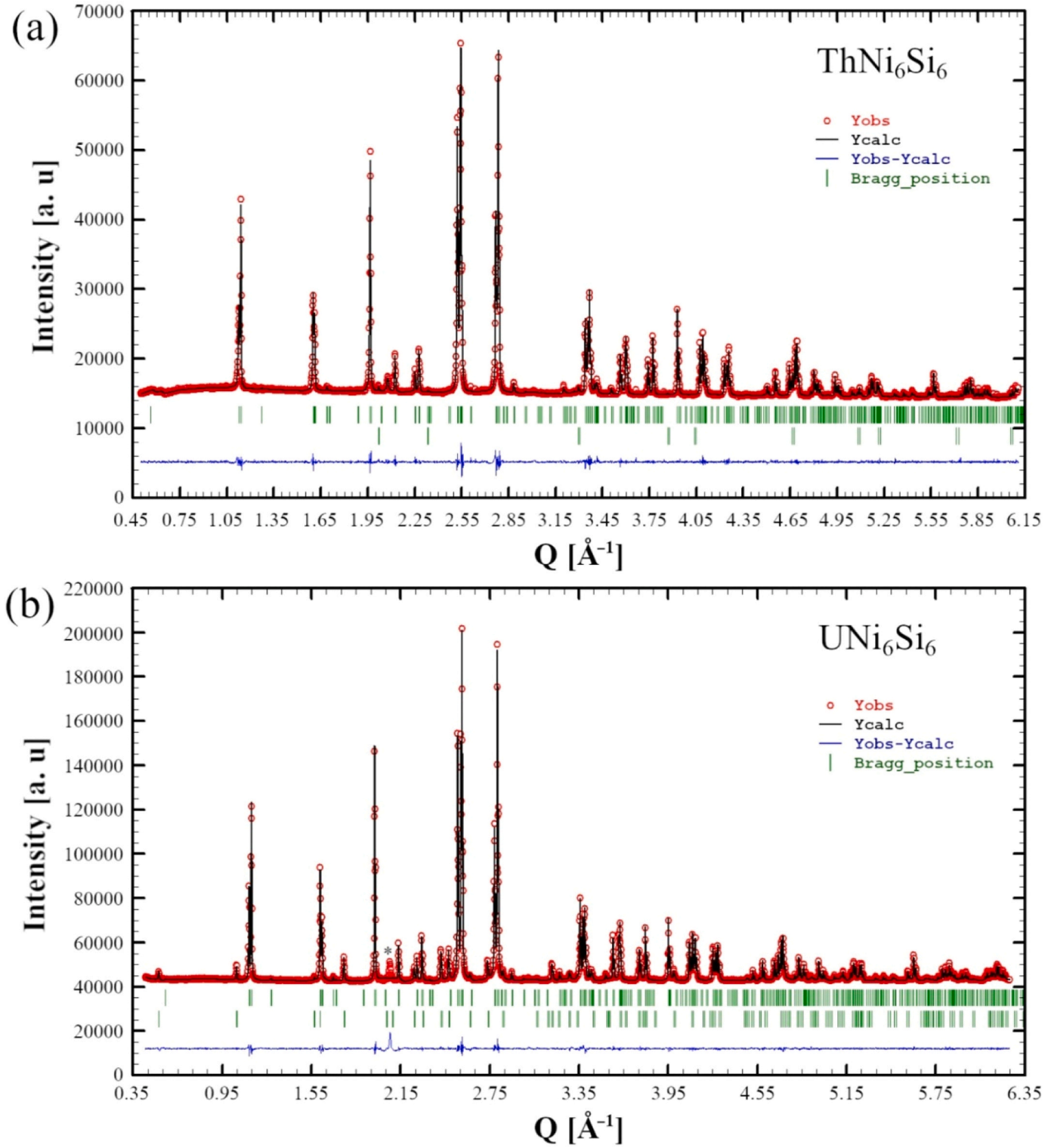

Fig. 5. Rietveld refinement plots for $ThNi_6Si_6$ (1000 °C - 7 days) (a) and UNi_6Si_6 (900 °C for 4 days + 1000 °C for 3 days) (b) by adopting the $CeNi_6Si_6$ structural model (space group *P4/nbm*, No. 125); the observed powder patterns are highlighted in red. The lower profile (blue line) gives the difference between observed and calculated data; the Bragg angle positions are indicated by vertical bars (green). The upper and low rows of Bragg positions for $ThNi_6Si_6$ indicate the $ThNi_6Si_6$ and $NiSi_2$ phases, respectively. The upper and lower rows of Bragg positions for UNi_6Si_6 pertain to the UNi_6Si_6 and UNi_2Si_3 compounds, respectively.

Curie constant $C_2 = 155(1) \bullet 10^{-5} \frac{emu \bullet K}{g \bullet Oe}$ and the temperature-independent term $\chi_0 = 7.3(3) \bullet 10^{-7} \frac{emu}{g \bullet Oe}$ for the pure UNi_6Si_6 phase. We can argue the following:

(i) the Curie-Weiss temperature is negative suggesting the presence of antiferromagnetic (AFM) correlations between U ions;
(ii) U ions do not magnetically order down to 2 K;
(iii) The Curie constant C_2 gives the effective moment $\mu_{eff} = 3.07(1)\ \mu_B$ for the U ions. Such value is lower than the expected one for the

Table 5
Agreement factors obtained after Rietveld refinements by adopting both the $CeNi_6Si_6$ (*P4/nbm*) and YNi_6Si_6 structural models ($P\bar{4}b2$) for both UNi_6Si_6 and $ThNi_6Si_6$ compounds.

	UNi_6Si_6		$ThNi_6Si_6$	
	$CeNi_6Si_6$-type	YNi_6Si_6-type	$CeNi_6Si_6$-type	YNi_6Si_6-type
	P4/nbm	$P\bar{4}b2$	*P4/nbm*	$P\bar{4}b2$
R_{Bragg} (%)	3.43	3.91	3.89	4.00
$R_{F\text{-}factor}$ (%)	3.84	4.21	4.55	4.81

Table 6
Structural data (standardized setting) for $ThNi_6Si_6$ ($CeNi_6Si_6$-type; *tP*52, *P4/nbm*, No. 125) as obtained by the Rietveld refinement.

Lattice parameters [Å]		$a = 7.8021(1)$				
		$c = 11.1636(1)$				
Unit cell volume [Å^3]		$V_{cell} = 679.56(1)$				
Atom	**Wyckoff site**	***x***	***y***	***z***	**Occ.**	**B_{iso} [Å^2]**
Th1	2*a*	1/4	1/4	0	1	0.63 (1)
Th2	2*b*	1/4	1/4	1/2	1	0.37 (1)
Ni1	8 *m*	0.6169 (1)	0.3831 (1)	0.0738 (1)	1	1.04 (1)
Ni2	8 *m*	0.5770 (1)	0.0770 (1)	0.3772 (1)	1	1.61 (1)
Si1	8 *m*	0.6318 (1)	0.1318 (1)	0.5783 (1)	1	0.99 (2)
Si2	8 *m*	0.5866 (1)	0.4134 (1)	0.8662 (1)	1	0.36 (2)
Ni3/ Si3	16 *n*	0.4457 (1)	0.1918 (1)	0.7578 (1)	0.50/ 0.50(1)	1.11 (1)

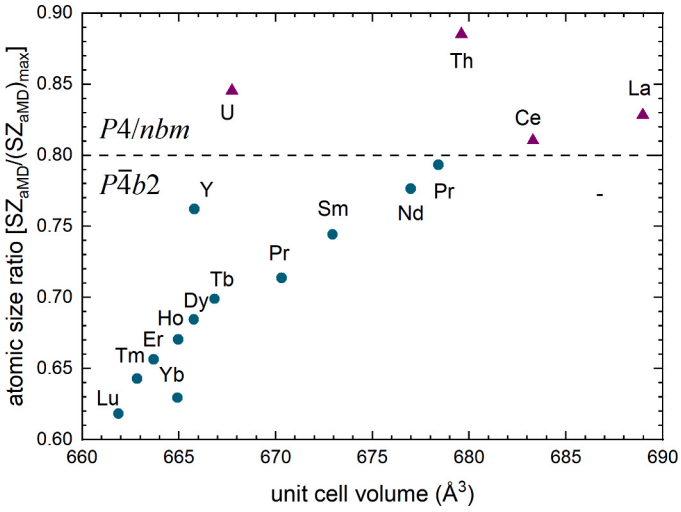

Fig. 6. Structural map for RNi_6Si_6 and $AcNi_6Si_6$ compounds (*Ac*: Th, U). The atomic size ratio is defined as $SZ_{aMD}/(SZ_{aMD})_{max}$ (see Villars *et al.* [19]).

free paramagnetic uranium ions U^{3+} or U^{4+} whose theoretical effective magnetic moments are $\mu_{eff}(U^{3+}) = 3.62\mu_B$ and $\mu_{eff}(U^{4+}) = 3.58\ \mu_B$, respectively. Analogous low effective free ion-magnetic moments were found in uranium intermetallic compounds in which the *5 f* states are located very close to the Fermi level and tend to be partially delocalized [20–25];

(iv) The temperature-independent term χ_0 could be ascribed to two possible different contributions: a Pauli-like paramagnetic component and/or a saturated ferromagnetic-like impurity present in an amount lower than the threshold of X-ray diffraction sensitivity (1 - 2%). The presence of such an impurity is supported also by the data of isothermal mass magnetization, M_m, measured at several temperatures ($T = 5$ K, 50 K, 120 K, 300 K) and presented in Fig. 8. These data show that the magnetization linearly decreases as a function of decreasing applied magnetic field, H, down to T = 50 K, as expected for a paramagnetic compound. Only the data measured at T = 5 K show a tiny curvature, which may be only ascribed to the above-mentioned ferromagnetic-like impurity.

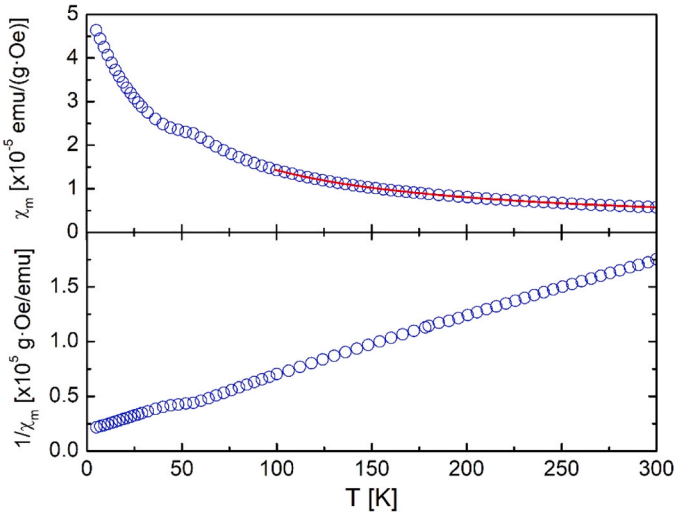

Fig. 7. Temperature dependence of the mass magnetic susceptibility χ_m for UNi_6Si_6 as measured with an applied magnetic field of 10 kOe. Upper panel: $\chi_m(T)$ and a two component Curie-Weiss fit above the magnetic transition of the spurious phase ($100K < T < 300K$). Lower panel: temperature dependence of $1/\chi_m(T)$. See text for details.

The isothermal mass magnetization, M_m, data for the $ThNi_6Si_6$ compound measured at $T = 120$ K and 300 K are shown in the left panel of Fig. 9, The two sets of data are almost superposed showing a negative (diamagnetic) slope almost *T*-independent. The temperature behavior of the mass susceptibility, χ_m, measured with an applied magnetic field H = 10 kOe is presented in the right panel of Fig. 9. The χ_m data show a small negative value almost *T*-independent down to 70 K, below which a $1/T$-like paramagnetic contribution appears. Such component is likely

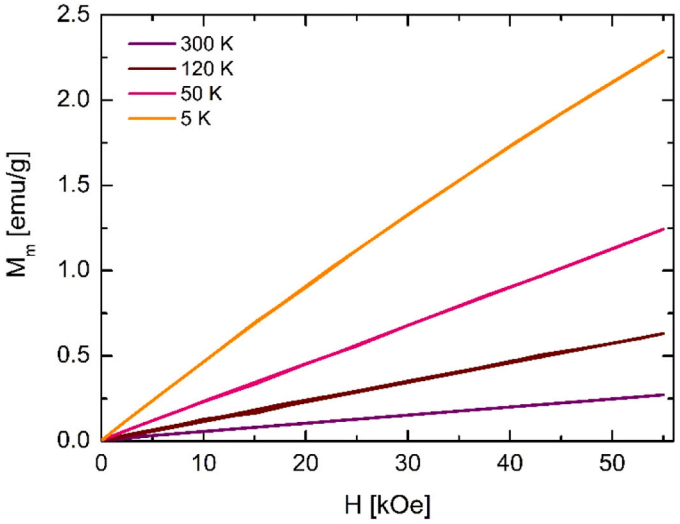

Fig. 8. Field-dependence of the mass magnetization, M_m, for UNi_6Si_6 measured at T = 5, 50, 120 and 300 K.

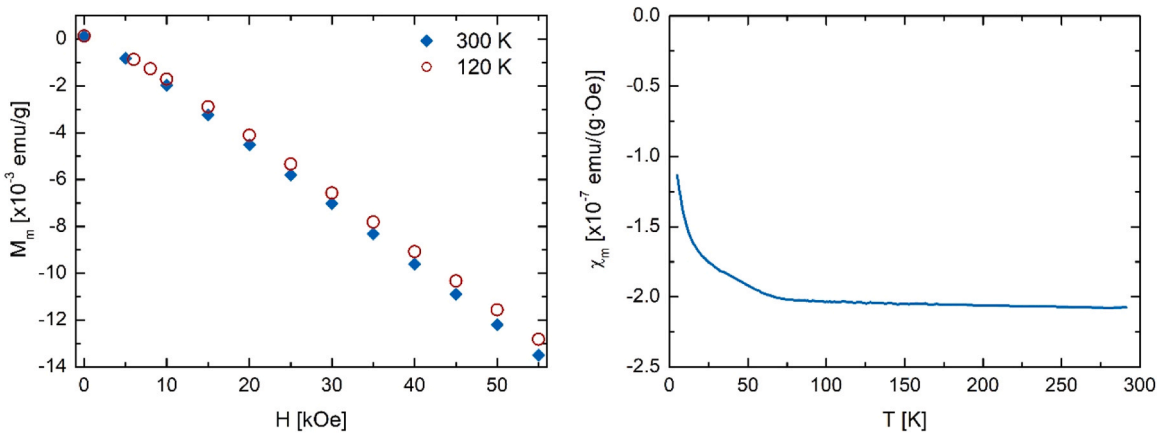

Fig. 9. Magnetic measurements for the $ThNi_6Si_6$ compound: field dependence of the mass magnetization, M_m, measured at T = 120 K and 300 K (left panel) and temperature-dependent mass susceptibility, $\chi_m(T)$, measured with an applied magnetic field H = 10 kOe (right panel).

ascribed to the presence of a small paramagnetic spurious phase, such as $NiSi_2$ [present in an amount of at least 1.0(1) vol% as detected by Rietveld refinement]. As a result, both $M_m(H)$ and $\chi_m(T)$ data indicate $ThNi_6Si_6$ compound is just weakly diamagnetic.

Fig. 10a shows electrical resistivity data of UNi_6Si_6. The data reveal a metallic behaviour for this compound, characterized by a monotonic decrease of the resistivity while decreasing the temperature. The temperature dependence of the resistivity of $ThNi_6Si_6$ (Fig. 10b) exhibits a metallic-like behavior as well. The Fig. 11 shows the resistances normalized to the room temperature value, R(*T*)/R(300 K), for both samples to compare their temperature dependence. In both compounds, the variation of the resistivity across temperature is moderate, but the UNi_6Si_6 sample reports a slightly higher residual resistivity ratio RRR=R (300 K)/R(10 K) of 1.6. It is worth to notice that neither in UNi_6Si_6 (for T ≥ 5 K) nor in $ThNi_6Si_6$ (for T ≥ 2 K), any superconducting transition is observed.

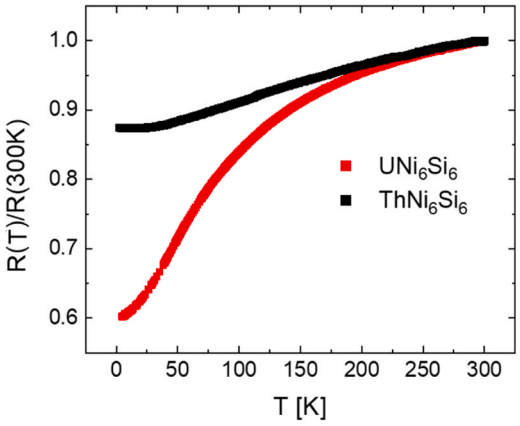

Fig. 11. Temperature dependence of electric resistance normalized to the room temperature value for UNi_6Si_6 and $ThNi_6Si_6$.

5. Conclusions

The crystal structure of the new UNi_6Si_6 and $ThNi_6Si_6$ intermetallic silicides has been determined by means of both single crystal (for the U compound only) and powder X-ray diffraction. Both compounds crystallize in the $CeNi_6Si_6$-type structure (*P4/nbm*, *tP*52) where one of the Wyckoff site is characterized by a disordered occupation of both Si and Ni atoms. This prototype is a ternary defect derivative of the binary $NaZn_{13}$-type, as determined by group-theoretical analysis. Magnetic susceptibility measurements reveal no magnetic order down to 2 K for both compounds. The temperature behavior of the mass magnetic susceptibility for UNi_6Si_6 was analyzed by using a two-component Curie-Weiss model; the fit gives a magnetic moment per formula unit lower than that expected for U^{3+} or U^{4+} free ions, this being likely due to a partial delocalization of U-*5 f* electrons. Analogous lower effective free ion magnetic moments have been reported in U intermetallic compounds in which the *5 f* states are located very close to the Fermi level

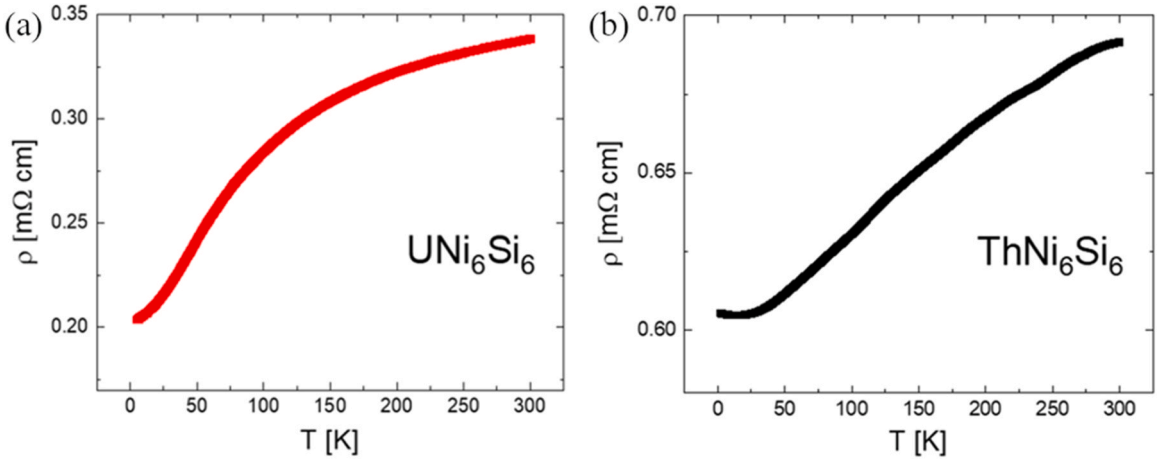

Fig. 10. Zero-field electrical resistivity as a function of temperature for UNi_6Si_6 (a) and $ThNi_6Si_6$ (b).

and tend to be partially delocalized. In the case of $ThNi_6Si_6$, the magnetic measurements show it to be diamagnetic. The electric resistivity shows a metallic behaviour for both compounds. Neither in UNi_6Si_6 (for $T \geq 5$ K), nor in $ThNi_6Si_6$ (for $T \geq 2$ K), a superconducting transition was detected.

CRediT authorship contribution statement

A. Martinelli: Formal analysis, Investigation, Writing - original draft, Review & Editing, Visualization. **G. Lamura:** Formal analysis, Investigation, Writing - original draft, Review & Editing. **P. Solokha:** Formal analysis, Investigation, Review & Editing. **A. Provino:** Formal analysis, Investigation, Review & Editing. **C. Bernini:** Formal analysis, Investigation. **M. Ceccardi:** Formal analysis, Investigation, Review & Editing. **M. Pani:** Review & Editing. **M. Ferretti:** Review & Editing. **S.K. Dhar:** Formal analysis, Investigation, Review & Editing. **P. Manfrinetti:** Conceptualization, Methodology, Formal analysis, Writing - review & editing, Supervision.

Declaration of Competing Interest

The authors declare that they have no known competing financial interests or personal relationships that could have appeared to influence the work reported in this paper.

References

[1] F. Steglich, J. Aarts, C.D. Bredl, W. Lieke, D. Meschede, W. Franz, H. Schäfer, Phys. Rev. Lett. 43 (1979) 1892–1896.
[2] H.R. Ott, H. Rudigier, Z. Fisk, J.L. Smith, Phys. Rev. Lett. 50 (1983) 1595–1598.
[3] M.W. McElfresh, J.H. Hall, R.R. Ryan, J.L. Smith, Z. Fisk, Acta Cryst. C 46 (1990) 1579–1580.
[4] P.K. Misra, Physics of Condensed Matter, Chapter 15, Heavy Fermions, in: Academic Press, 2011, p. 509.
[5] M. Wendorff, C. Röhr, J. Alloy. Compd. 421 (2006) 24–34.
[6] M. Pani, P. Manfrinetti, A. Provino, Fang Yuan, Y. Mozharivskyj, A.V. Morozkin, A. V. Knotko, A.V. Garshev, V.O. Yapaskurt, O. Isnard, J. Solid State Chem. 210 (2014) 45–52.
[7] A.V. Morozkin, A.V. Knotko, A.V. Garshev, V.O. Yapaskurt, R. Nirmala, S. Quezado, S.K. Malik, J. Solid State Chem. 243 (2016) 290–303.
[8] G.R. Stewart, J. Low. Temp. Phys. 195 (2019) 1–25.
[9] Bruker, APEX4 V2021.10-0, Bruker AXS Inc., Madison, Wisconsin, USA, 2021.
[10] Bruker, SAINT v8.30A, Bruker AXS Inc., Madison, Wisconsin, USA, 2012.
[11] Bruker, XPREP V2014/2, Bruker AXS Inc., Madison, Wisconsin, USA, 2014.
[12] Bruker, SADABS V2016/2, Bruker AXS Inc., Madison, Wisconsin, USA, 2016.
[13] G.M. Sheldrick, SHELXL-2019/1, Bruker AXS Inc., Madison, Wisconsin, USA, 2019.
[14] K. Yvon, W. Jeitschko, E.J. Parthé, Appl. Crystallogr. 10 (1977) 73–74.
[15] J. Rodriguez-Carvajal, Physica B 192 (1993) 55–69.
[16] P. Müller, Crystal Structure Refinement: A Crystallographers Guide to SHELXL, Oxford University Press, 2006.
[17] P. Villars, J.L.C. Daams, J. Alloy. Compd. 197 (1993) 177–196.
[18] L.G. Akselrud, Visn. Lviv. Derzh. Univ., Ser. Khim. 23 (1981) 33–38.
[19] P. Villars, J. Daams, Y. Shikata, K. Rajan, S. Iwata, Chem. Met. Alloy. 1 (2008) 1–23.
[20] J. Grunzweig-Genossar, M. Kuznietz, F. Friedman, Phys. Rev. 173 (1968) 562–573.
[21] M. Pasturel, M. Szlawska, J. Ćwik, D. Kaczorowski, A.P. Pikul, Intermetallics 131 (1-7) (2021), 107112.
[22] M.S. Henriques, O. Tougait, H. Noel, L.C.J. Pereira, J.C. Waerenborgh, A. P. Gonçalves, Solid State Comm. 148 (2008) 159–162.
[23] F. Canepa, A. Palenzona, R. Eggenhoffner, Physica B 160 (1990) 297–303.
[24] R. Eggenhoffner, F. Canepa, A. Palenzona, J. Alloy. Compd. 178 (1992) 125–129.
[25] A. Amorese, M. Sundermanna, B. Leedahl, A. Marino, D. Takegami, H. Gretarsson, A. Gloskovskii, C. Schlueter, M.W. Haverkort, Y. Huange, M. Szlawska, D. Kaczorowski, S. Rang, M.Brian Maple, E.D. Bauer, A. Leithe-Jasper, P. Hansmann, P. Thalmeier, L.H. Tjeng, A. Severing, PNAS 117 (2020).